

## Shallow S-Wave Velocity Structure from Ambient Seismic Noise at Planchón-Peteroa Volcanic Complex, Argentina-Chile

Casas, Augusto; Mikesell, D; Draganov, Deyan; Lepore, Simone; Badi, Gabriela; Franco, Luis; Gomez, Martin

**DOI**

[10.1785/0120170281](https://doi.org/10.1785/0120170281)

**Publication date**

2018

**Document Version**

Accepted author manuscript

**Published in**

Bulletin of the Seismological Society of America

**Citation (APA)**

Casas, A., Mikesell, D., Draganov, D., Lepore, S., Badi, G., Franco, L., & Gomez, M. (2018). Shallow S-Wave Velocity Structure from Ambient Seismic Noise at Planchón-Peteroa Volcanic Complex, Argentina-Chile. *Bulletin of the Seismological Society of America*, 108(4), 2183-2198. <https://doi.org/10.1785/0120170281>

**Important note**

To cite this publication, please use the final published version (if applicable). Please check the document version above.

**Copyright**

Other than for strictly personal use, it is not permitted to download, forward or distribute the text or part of it, without the consent of the author(s) and/or copyright holder(s), unless the work is under an open content license such as Creative Commons.

**Takedown policy**

Please contact us and provide details if you believe this document breaches copyrights. We will remove access to the work immediately and investigate your claim.

# Shallow *S*-Wave Velocity Structure from Ambient Seismic Noise at Planchón-Peteroa Volcanic Complex, Argentina-Chile

by José Augusto Casas, T. D. Mikesell, D. Draganov, S. Lepore,  
G. A. Badi, L. Franco, and M. Gómez

**Abstract** We applied the seismic interferometry technique to characterize the subsurface velocities of the Planchón-Peteroa Volcanic Complex, Argentina-Chile, down to a depth of about 350 m. Ambient seismic noise data were recorded by an array of six stations deployed in the eastern flank of the current active volcano of this volcanic complex—the Peteroa. To ensure retrieval of accurate surface-wave Green’s functions, we analyzed the directivity of the recorded ambient noise and then selected the noise windows containing source directions in line with the stationary-phase area for each station pair. Then, we obtained dispersion curves and further utilized them for the estimation of the *S*-wave velocity profile for the area enclosed by the stations.

We inferred two layers above the investigation depth limit. In the first 70 m, a low-velocity layer (300–400 m/s) is present, which is followed by a higher velocity layer (450–570 m/s) down to, at minimum, a depth of about 350 m. Higher velocities are observed at the northeast and the very southwest of the area under investigation, and lower velocities are observed between these areas. The *S*-wave velocity structure is consistent with the known near-surface lithologies of the area. The results along the western side of the area corroborate previous results obtained from geochemical studies. Velocity variations in the area are potentially caused by changes in lithology, porosity, and water saturation. This work contributes to the understanding of the subsurface of Peteroa volcano and provides useful information to the authorities for decision-making. Furthermore, these results are expected to be used by studies preceding risk analysis and hazard-assessment investigations.

## Introduction

In active volcanic areas, one of the main goals of local governments and the scientific community is to reduce the risk experienced by nearby populations (Loughlin *et al.*, 2015). This goal is achieved mainly through accurate monitoring of the dynamic volcano system. In particular, seismic monitoring could increase the knowledge of the subsurface properties and structures, which improves the forecasting performed by volcano observatories. This forecasting, in turn, influences the strategies adopted by the authorities.

The Planchón-Peteroa Volcanic Complex (PPVC; 35.24° S, 70.57° W, and 3603 m.a.s.l.) is located in the Andes, along the Argentina–Chile border (see Fig. 1). In particular, PPVC is located in the Transitional South Volcanic Zone, a region characterized by an angle of subduction ranging approximately between 30° and 35°, providing appropriate temperature and pressure conditions on the subducting plate for the development of magmas at depths between 100 and 200 km (Gill, 1981). In this area, northwest–southeast and northeast–southwest fault systems enable ascent and emplacement of magma, as well as spatially constrain the location of

calderas, stratovolcanoes, and geothermal activity, and, as a consequence, the genesis of the PPVC (Cembrano and Lara, 2009).

During the last 7000 yrs, volcanic activity was concentrated in several scattered vents, which gave rise to Peteroa volcano (Tormey *et al.*, 1989; Haller *et al.*, 1994). Historical activity records of Peteroa volcano expose about 20 eruptive events, most of them weak. Based on analyses of the tephra deposited in the area of the PPVC, Naranjo (2012) characterized the observed volcanic activity between 4 September and November 2010 as an indication of a system reactivation. Currently, a hydrothermal system fed by a melting ice cap and infiltrating groundwater is present in the area of PPVC. The interaction of this system with rocks heated by the shallowest part of the magma chamber (about 4 km depth) could explain the periods of volcanic unrest (Benavente Zolezzi, 2010). Aguilera *et al.* (2016) characterized the physical processes that occurred during and after the eruptive period 2010–2011 by means of an analysis of fall deposits and geochemical samples from fumaroles and crater



**Figure 1.** Northern section of the South Volcanic Zone (SVZ) and the developed volcanic edifices. The white star indicates the Planchón-Peteroa Volcanic Complex (PPVC). The white dots show the location of populated and touristic points approaching the volcanic complex. The Chile–Argentina international border is indicated with a thick contour. The color version of this figure is available only in the electronic edition.

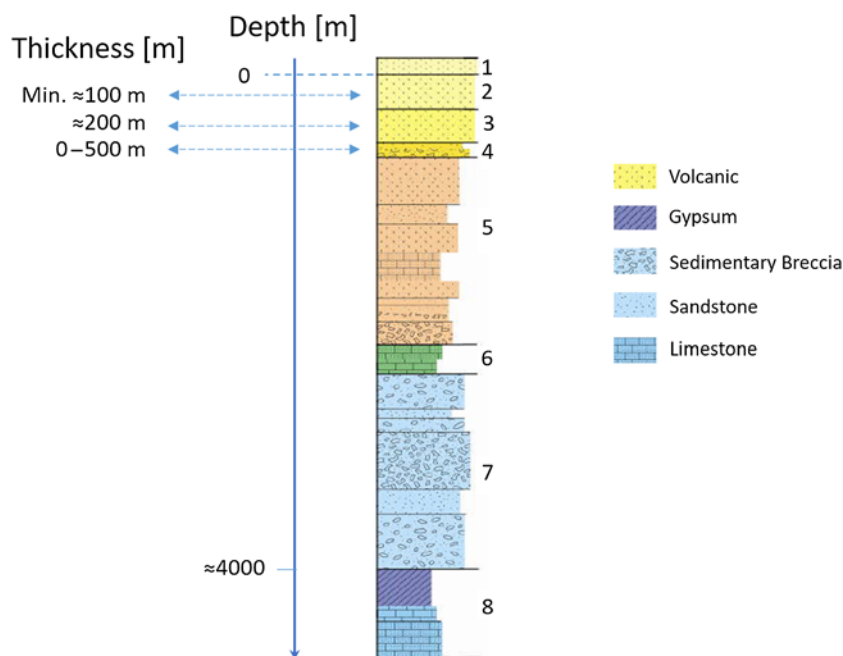


**Figure 2.** Stratigraphic column for the area of the PPVC. Units: 1, Loma Seca; 2, Volcán Peteroa-Azufre; 3, Cola de Zorro; 4, Estratos del Colorado; 5, Abanico; 6, Debia; 7, Rio Damas; and 8, Valle Grande. The thicknesses and identification of the layer exposed at the surface of the area (0 m depth) are from [Tapia Silva \(2010\)](#) and [Lemus Hernandez \(2010\)](#). Modified from [Lemus Hernandez \(2010\)](#). The color version of this figure is available only in the electronic edition.

lakes. They suggest two possible physical mechanisms that caused the 2010–2011 volcanic unrest: the development or reactivation of cracks after the  $M_w$  8.8 Maule earthquake in February 2010, which caused the escape of fluids and heat from a shallow magmatic-hydrothermal reservoir; or an instability produced by a reduction of fluid pressure within the shallow reservoir could have caused a rupture of the seal zone

that confined an underlying magma chamber, causing phreatic eruptions ([Fournier, 2007](#)).

[Lemus Hernandez \(2010\)](#) characterized the geology in the area of the PPVC and provided a general stratigraphic column down to  $\sim 5$  km depth (see Fig. 2). From the shallowest stratigraphic units, those relevant to our study area are the Volcán Peteroa-Azufre unit and the Cola de Zorro formation. The first is exposed at the surface of the studied area ([Tapia Silva, 2010](#)); it is composed of eroded lavas and pyroclastic rocks (basaltic, dacitic, and andesitic material) deposited in a layer of variable thickness (a minimum of  $\sim 100$  m). The next unit is the Cola de Zorro formation, a layer  $\sim 200$  m thick composed of andesitic–basaltic volcanic material.

[Tassi et al. \(2016\)](#) analyzed the fluid manifestations at the summit and surrounding the Peteroa volcano for the period 2010–2015. They propose that the composition of the geochemical samples is induced by the presence of two magma batches emplaced at different depths; that is, a shallow dacitic reservoir and a deeper basaltic reservoir. Depending on the date of the measurements, the composition of the samples collected at the summit related to one or the other of the magmatic sources emplaced below. Bubbling pools and a shallow aquifer fed by water vapor condensation and rain and glacier melting are present on the eastern flank of the PPVC. Gases from the bubbling pools are characterized by a small magmatic fluid contribution, which could suggest a proximity to a magma reservoir. The likely presence of magma approaching a subsurface saturated by water warrants study of the area.

Currently, Peteroa volcano and its nearby surroundings are being monitored by permanent seismic stations, real-time camera observations, Global Navigation Satellite System,  $SO_2$ , and diffuse  $CO_2$  measurements (Volcanic Activity Reports,

Observatorio Volcanológico de los Andes del Sur, Chile; [Agusto et al., 2017](#); [Raponi et al., 2017](#)). This information is directly available to the local municipality, which would help facilitate timely decisions about the general condition of volcanic activity, the information to be distributed to scientists and the community, the assignments to personnel, and the deployment of extra recording instruments, among other decisions. Knowledge of the structures and processes

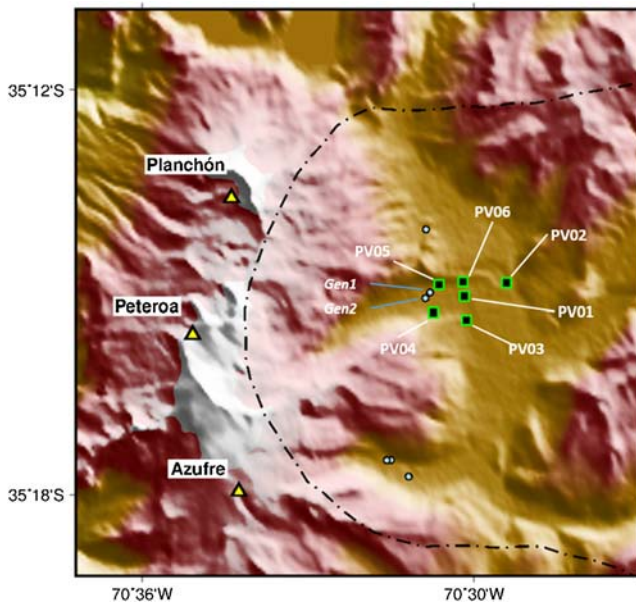


**Figure 3.** Station distribution (squares) and their names (PV01–PV06) in relation to the main volcanic features of the PPVC (triangles). The Chile–Argentina international border is displayed with a dashed line. The circles indicate points of thermal manifestations (based on Benavente *et al.*, 2015, and Tassi *et al.*, 2016). In particular, the name of those points approaching the PV-array (Gen1 and Gen2) were included. The color version of this figure is available only in the electronic edition.

occurring in the subsurface, via seismic observations, will further contribute to the interpretation of this volcanic complex, thus aiding the above-mentioned decisions.

To investigate the subsurface structure and develop an understanding of possible subsurface phenomena, we imaged the seismic velocity structure in the area using ambient-noise tomography. Ambient-noise tomography is a widely-used tool in volcanic environments (e.g., Brenguier *et al.*, 2007; Stankiewicz *et al.*, 2010; Escudero and Bandy, 2017). This method applies seismic interferometry (SI) to recorded ambient noise to retrieve (ballistic, i.e., direct) surface-wave arrivals between station pairs. The retrieved arrivals are then used for an interstation tomography between all station pairs. We use ambient-noise seismic data recorded by stations deployed at the Argentinian flank of the Peteroa volcano (see Fig. 3) to retrieve the *S*-wave velocity distribution for the area enclosed by the stations. From January 2012 to January 2013, the temporary MalARRgue network (Rui-grok *et al.*, 2012; Nishitsuji *et al.*, 2014) recorded data at 38 seismic stations in the Malargüe region, Mendoza Province, Argentina. The main goal of this project was to image and monitor the subsurface below the region. Six of these stations (hereafter, the PV-array) were located near the international border; that is, along the eastern flank of the Peteroa volcano, and thus selected for this study. The PV-array stations consist of short-period (2 Hz) three-component Sercel L-22 sensors. The close distribution of the PV-array (i.e., an interstation distance ranging between 0.4 and 2.1 km) provides high

coherency for the recorded signals among the stations, which is essential to ensure the accuracy of the results.

Theoretical studies have shown that the cross correlation of wavefields at two receivers can provide an estimate of the Green’s function (GF) for propagation in the subsurface between these receivers (e.g., Snieder, 2004; Wapenaar and Fokkema, 2006). This technique has been called SI (Schuster, 2009). Diffuse wavefields such as coda waves from seismic events (Campillo and Paul, 2003) or long seismic noise records (Shapiro and Campillo, 2004) are used to estimate the surface-wave part of the GF. This information is then used with traditional methods developed for inversion of surface-wave data to characterize the subsurface. Surface-wave group velocities can be retrieved as a function of frequency and subsequently inverted to estimate the *S*-wave velocities as a function of depth (Bensen *et al.*, 2008).

The assumption of a diffuse noise wavefield is not always appropriate (Godin, 2006; Mulargia, 2012). In many practical situations, noise wavefields show clear evidence of dominant directions of propagation, that is, directionality. The directionality could affect the constructive interference of energy from inside the stationary-phase area (i.e., the Fresnel zone), which contributes to the retrieval of the GF, and the destructive interference from outside that area (Snieder, 2004). The incomplete destructive interference of contributions from sources located outside the stationary-phase area for a station pair leads to the presence of spurious events in the retrieved GFs (e.g., Xu and Mikesell, 2017). In the case of nonisotropic noise, proper selection of the noise sources to be used for processing is crucial for a correct estimate of the propagation velocities (Wapenaar and Thorbecke, 2013).

The noise-wavefield directionality varies with frequency; for the higher frequencies, the spatial and temporal variability of the seismic sources could be more complex. Several studies (e.g., Halliday *et al.*, 2007; Picozzi *et al.*, 2009) have shown the applicability of SI to a frequency range higher than that conventionally used for regional- and global-scale studies (i.e., the primary [0.05–0.08 Hz] and secondary microseism [0.1–0.16 Hz]). Thus, we overcome the issue of directionality of the noise sources by selecting time periods for which the seismic noise energy predominantly arrives from the expected stationary-phase area for each station pair, and apply SI to these selected times.

Here, we aim to contribute to the knowledge of the subsurface at PPVC. Using the records of ambient seismic noise, we retrieved the surface-wave part of the GFs, and from that estimate the surface-wave group velocity distribution in the area enclosed by the stations. A depth inversion is applied to provide the distribution of the *S*-wave velocities with depth. Finally, a geological interpretation is performed based on the *S*-wave velocity results, the available lithological information, and the fluid manifestations in the studied area.

## Data Processing

Because short-period (2 Hz) stations were utilized, the deconvolution of the instrument response constitutes the first step of the processing procedure. Despite the corner frequency of 2 Hz, comparative analyses with broadband sensors prove that accurate amplitudes are still obtained down to 0.1 Hz, given that the data are corrected for the instrument response (Weemstra *et al.*, 2017). Therefore, we deal with accurate ground velocity spectral amplitudes, which allows us to carefully select the frequency range for further processing of the data and to perform the polarization analysis; these two processing steps are detailed below in this section. Because the data were recorded by the same type of instruments, a correction for the instrument response is not necessary for the computation of the cross correlations. Nevertheless, the instrument response was corrected, and we proceeded to use the deconvolved traces also for the computation of the cross correlations because the obtained dispersion curves (DCs) do not suffer from such processing.

To retrieve an accurate estimate of the desired parts of the GFs, all the noise sources must be illuminating the stations with equal energy levels (Draganov and Ruigrok, 2015). If this is not the case, information from weaker sources is lost in the averaging process, thus creating illumination gaps and resulting in erroneous GF retrieval. Therefore, normalizing the amplitude of the recorded noise will homogenize the energy contributions. Similarly, the presence of recurrent narrowband sources can deteriorate the cross correlations and consequently the estimated GFs (Bensen *et al.*, 2007). To overcome these issues, we applied a time-frequency spectral normalization (Shen *et al.*, 2012).

We performed spectral analysis to select the useful frequency range. For this, we computed functions of power spectral density (PSD). Only a limited range of wavelengths can be used for an accurate estimation of the GFs (Bensen *et al.*, 2007; Picozzi *et al.*, 2009). For each station pair, we used wavelengths shorter than the interstation distance. Based on the PSD values between the different frequency bands and the interstation distances, the frequency band between 0.8 and 4 Hz was selected. As an example, Figure 4 shows the PSD for one of the stations (PV06) for 45 days (1 March–16 April 2012). The general spectral features are similar over the stations and roughly sustained over the entire recording period (Casas *et al.*, 2014).

Several seismic sources located in the area of the PPVC influence the noise records at the stations. The origin of the main noise sources present near the studied area may be related to tectonic seismicity, ocean waves, meteorological effects, volcanic processes, running brooks, and anthropogenic activity. The seismic energy from these contributions changes in space and time, particularly when the working range of frequencies of interest is higher than that commonly used in seismology for regional-scale tomographic studies (less than 1 Hz, Bonnefoy-Claudet *et al.*, 2006; Picozzi *et al.*, 2009). An in-depth analysis of the types of sources present in

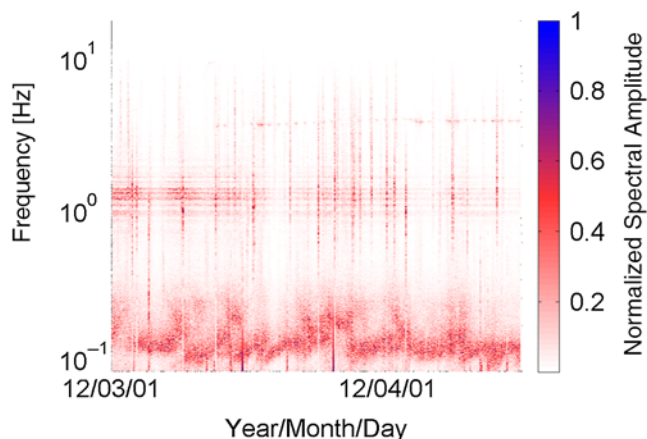


**Figure 4.** Power spectral density (PSD) function calculated for the period 1 March–16 April 2012, for one of the stations (PV06) located in the area of the PPVC during 2012. The spectral amplitudes were normalized by the maximum amplitude during this period of time. The color version of this figure is available only in the electronic edition.

the area over the frequency range of interest and of their temporal and spatial variability is beyond the scope of this work; however, the knowledge of the dominant directions of the noise wavefield over time is essential for an accurate retrieval of the empirical GF (Mulargia, 2012; Wapenaar and Thorbecke, 2013; Nakata *et al.*, 2016). We estimated the directivity of the noise wavefield over the recording period using the degree of polarization (DOP) method (Schimmel and Gallart, 2004).

The DOP is an alternative to techniques more generally used in seismology (e.g., beamforming), which sometimes do not provide reliable results due to the array geometry and/or the frequency range of interest. DOP allows the identification and enhancement of polarized signals arriving to a station while suppressing less polarized signals (i.e., enhancing certain directions and suppressing others, which means that it analyzes the illumination directions). Once illumination directions are obtained at each of the stations, a joint interpretation is performed across the array to estimate the directivity of the noise incident at the array.

We applied DOP to nonoverlapping windows over the entire recording period. An analysis to select the window length (i.e., number of days) was performed. We used windows of different lengths and analyzed which window would be appropriate to identify the main spatiotemporal changes of the wavefield. Our analysis showed that a trade-off between two effects is present. Using short windows led to the dominance of low-repeatability sources, that is, noise sources that illuminated a certain receiver pair incidentally. On the other hand, a large window downweighs the effect of several sources; that is, if several noise sources illuminate the array along different paths, the strongest will dominate while the others will be suppressed. After performing tests with different lengths, we chose 14 days as the window length in the directional estimate of the noise, as seismic energy among

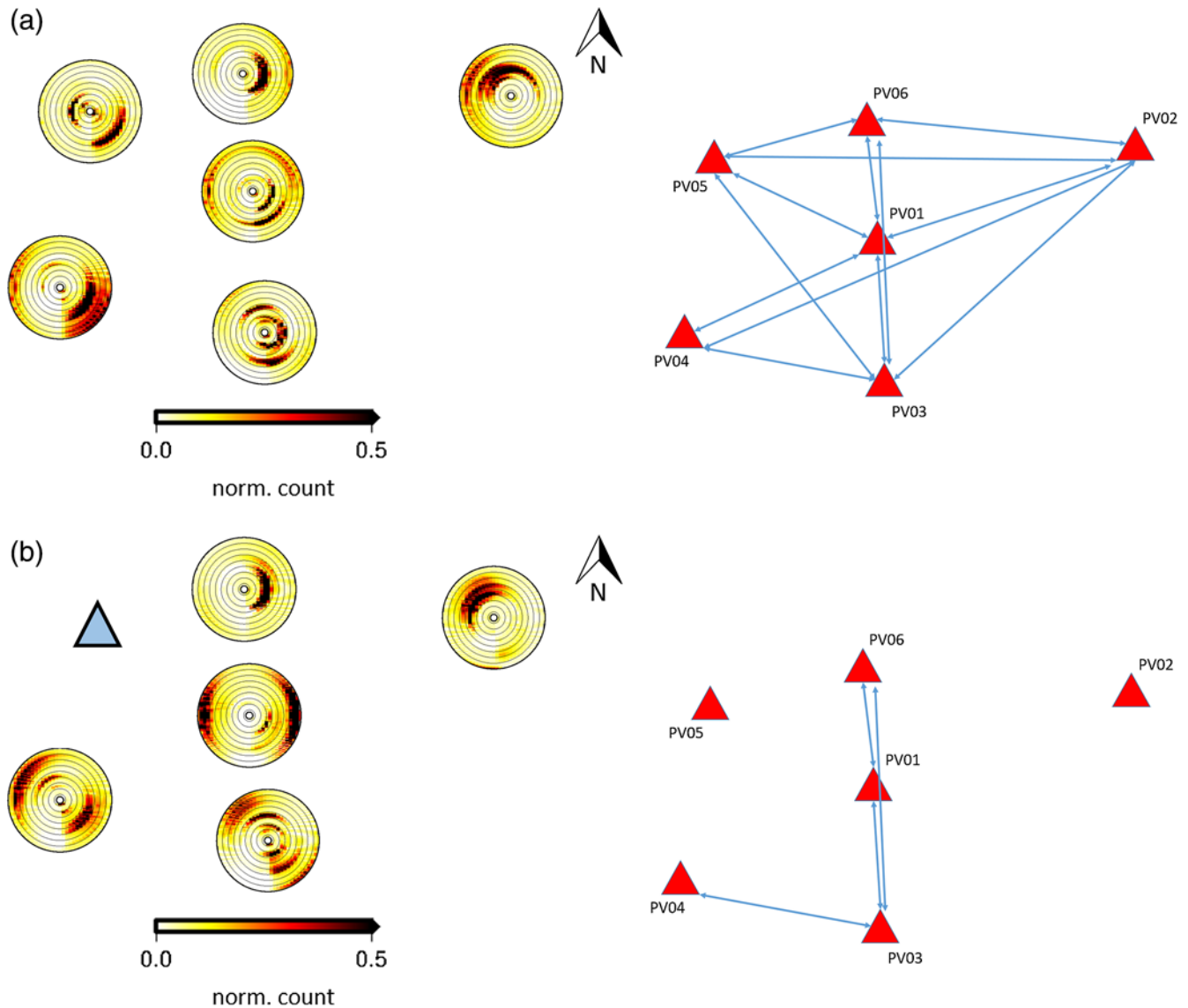


**Figure 5.** Estimate of the dominant direction of the noise wavefield by application of a polarization analysis for (a) 11–24 January 2012 and (b) 4–17 April 2012. For every station, results are shown by a polar illustration in which the angle relative to the north direction represents the back azimuth ( $0^{\circ}$ – $360^{\circ}$ ), and the radius represents the frequency values (0.3–4.5 Hz, moving from the center out, respectively). Note that the palette for the normalized amplitudes saturates for values higher than 0.5. The right plot indicates the selected station pairs (connected with lines). Nonactive stations for the period of interest are shown with triangles in the left plot. The color version of this figure is available only in the electronic edition.

the subsequent windows are satisfactorily coherent. The results of DOP for two of the windows are shown in Figure 5: the left plot shows the results for every station, and the right plot indicates the selection of the station pairs with sources in the stationary-phase area (arrows). This selection was performed by an estimation of the dominant directions of the noise wavefield, which are indicated by a significant number of DOP values higher than 0.5. A time interval for a station pair is selected for further processing; that is, averaging, if energy propagates along the line that passes through those stations for frequencies inside the frequency band [0.8, 4] Hz, even if a nonnegligible amount of energy is present along other directions. Based on the linearity values calculated by the

algorithm, we estimate the uncertainty in the directivity results at around  $8^{\circ}$  (De Meersman *et al.*, 2006). Thus, we select the station pairs for which the connecting line differs in less than  $8^{\circ}$  from a dominant direction of illumination for that station pair. For example, the station pair PV05–PV06 is selected for the period presented in Figure 5a, but not the station pair PV04–PV05; the station pair PV01–PV06 is selected for the period presented both in Figure 5a and 5b because, taking into account the  $8^{\circ}$  uncertainty, the path connecting the two stations crosses (the corners of) a dominant illumination direction.

Averaging all of the selected periods for each station pair allows us to say that the polarization analysis (i.e., directivity) helped improve the energy level of the signals along the

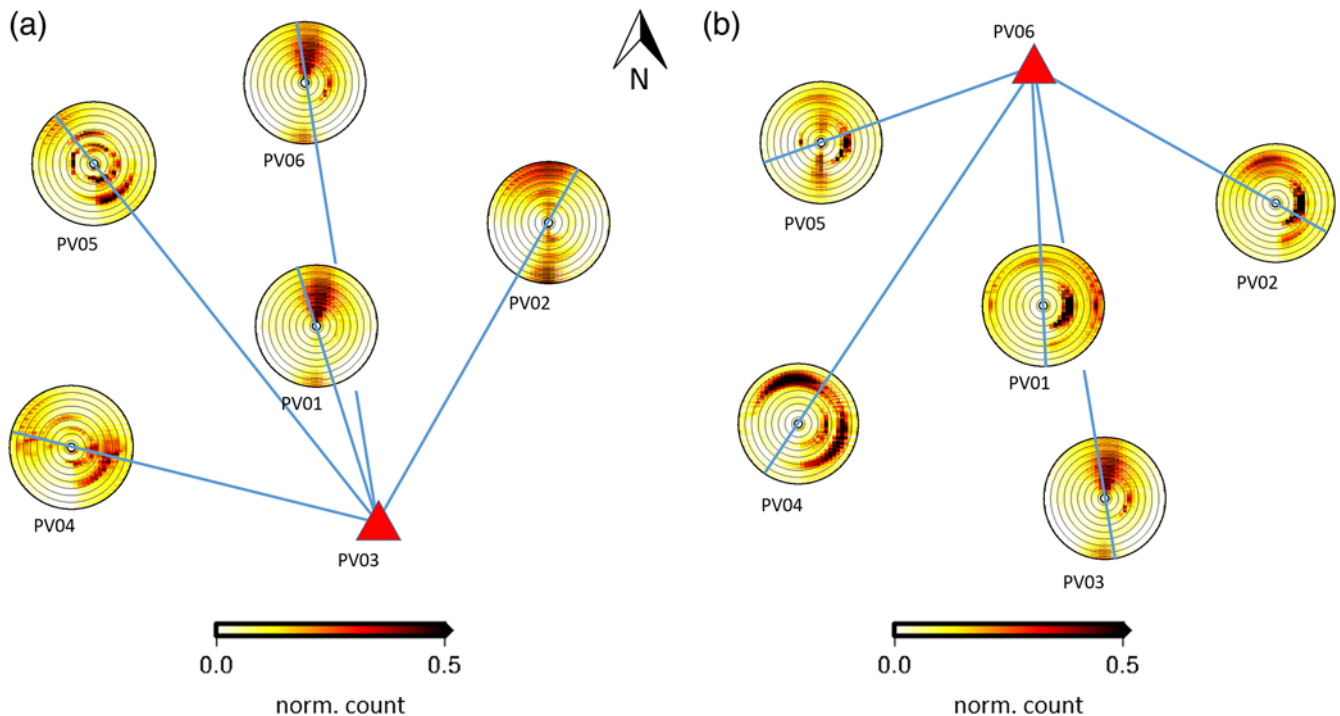


**Figure 6.** Averaged degree of polarization (DOP) results for (a) PV03 and (b) PV06. The averaging was performed using only the time intervals that were selected as containing seismic energy along the line of interest. Straight lines display the back azimuth of the station pairs of interest. The color version of this figure is available only in the electronic edition.

directions of interest of the noise wavefield. Figure 6a and 6b shows the average plots for the station pairs related to PV03 and PV06, respectively. One should note that some energy is still aligned with out-of-line directions, likely degrading the quality of the calculated GFs. Nevertheless, on the whole, propagation energy aligned with the stations is dominant.

The GF for a pair of stations is retrieved by cross correlating the records at two stations. In this work, the above-mentioned instrument deconvolution and data normalization procedures were applied to time windows of 1-hr length and then stacked after cross correlation to obtain daily GFs. It is important to note that a daily GF was computed only for days during which the considered station pair was aligned with a dominant direction of the noise wavefield. In this way, we ensure that we preferentially consider sources in the stationary-phase region for the accurate retrieval of the ballistic surface-wave part of the GFs. As for the retrieval of the surface-wave part of the GFs, we used the vertical-component recordings of the stations, because this way the retrieved waves will be Rayleigh waves. The obtained full-band (i.e., [0.8, 4] Hz) GFs are organized by interstation distance and shown in Figure 7. The spatial dependence of the surface-wave velocity due to the highly heterogeneous nature of volcanic areas could explain the variation in arrival times for the different interstation distances (and azimuths). The gray rectangles, which are only illustrative, delimit the time required for retrieved ballistic surface waves to traverse the distance between each station pair. For this illustrative purpose, we used velocities between 0.2 and 0.8 km/s to estimate expected

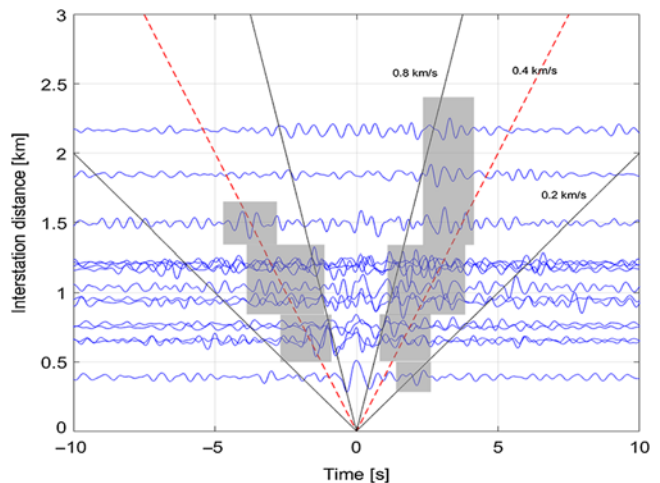


**Figure 7.** Retrieved Green's functions for the station pairs in the PV-array organized by interstation distance. Straight lines denote constant velocities as a reference and gray-shaded rectangles display the times at which retrieved surface waves arrive. Dashed lines represent the estimated average surface-wave velocity for the area enclosed by the stations (see the Appendix). The color version of this figure is available only in the electronic edition.

arrival times. We also utilized shallow local earthquakes (with epicentral distances less than 350 km) to estimate the average surface-wave velocity for the area of the PV-array (see the Appendix for details). The obtained average surface-wave velocity of 0.4 km/s coincides with that obtained from the

ambient noise (see Fig. 7). Figure 7 also shows nonnegligible amplitudes at shorter times, that is, high velocities. These higher velocity waveform amplitudes may be due to seismic energy propagating (nearly) perpendicularly to the line that passes through the stations involved but could not be attenuated due to insufficient destructive interference.

The causal part of the GFs (i.e., amplitude values for the positive times of the seismogram) is shaped by the seismic energy propagating from the virtual source toward the receiver. Similarly, the acausal part of the GFs (i.e., the negative times) is shaped by the seismic energy that propagates from the receiver toward the virtual source. Thus, the noise sources behind both stations are used to construct the causal and the acausal part of the GFs. To retrieve both times with the same amplitude, the noise from both directions (from source to receiver and from receiver to source) should be at the same energy level. But even in such a case, persistent energy propagating along a direction other than these two might cause interference with the retrieved causal or acausal surface-wave arrivals and make it appear to be at an earlier or later time. Another case of inequality is when, for example, the energy from the source to the receiver propagates along the line connecting the two, while the energy propagating from the receiver to the virtual source make a small angle with that line. In this case, the retrieved surface wave at acausal times will appear at an earlier time. Both of the above cases are caused by not having omnidirectional illumination of the station pair and, thus, insufficient destructive interference outside the stationary-phase zone (e.g., Wapenaar and Thorbecke, 2013; Xu and Mikesell, 2017).

The dispersion of surface-wave energy is commonly exploited to estimate the *S*-wave velocities of the medium through which the surface-wave energy propagates (Aki and Richards, 1980; Xia *et al.*, 1999; Haney and Tsai, 2017). A surface-wave DC provides information on the surface-wave velocity values as a function of frequency for a given station pair. Based on the retrieved GFs, we made use of the causal, acausal, or summed causal and acausal part of the trace for the calculation of the DC. This analysis provides the opportunity to filter out out-of-line directions of the noise wavefield. The choice of which part to use was done separately for each station pair and based on the analysis of the dominant directions of the noise wavefield. For a station pair, we chose the causal part when the dominant noise direction is from the virtual source to the receiver. When the dominant noise direction is from the receiver to the virtual source, we chose the acausal part. When the noise illumination from both directions, as described above, is comparable, we sum the causal and acausal part. We obtained the group-velocity DCs for the retrieved ballistic surface-wave part of the GFs through the measurement of the arrival time of the propagated energy after application of several narrowband filters (e.g., Bensen *et al.*, 2007). An example of a group-velocity DC for one of the station pairs is shown in Figure 8. The computation of the error bars is based on the analysis of the energy distribution in the frequency–velocity field. Clear maximum amplitudes

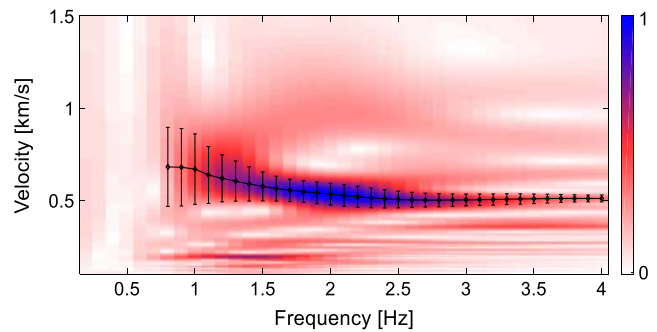


**Figure 8.** Dispersion curve obtained for the station pair PV02–PV04. In this example, the interstation distance is 2.16 km. The color version of this figure is available only in the electronic edition.

in the field provide lower errors than those in which the maximum amplitudes spread over a relatively large area of the frequency–velocity field.

### Rayleigh-Wave Tomography

To estimate the Rayleigh-wave velocities as a function of frequency for the area enclosed by the stations, we performed tomographic inversion using the software PRONTO (Aldridge and Oldenburg, 1993). PRONTO uses an iterative tomographic inversion procedure based on a ray-tracing algorithm and finite-difference travel-time computations. Its advantages are the accurate and rapid computation of forward models and the incorporation of constraints to the inverse solution from geological or geophysical information. To improve the stability of the procedure, this algorithm applies linear equality constraints to the slowness model, instead of to model perturbation at each iteration. We also imposed a smoothness constraint on the results. Using a background velocity model as a reference, smoothing weights are defined in the objective function, and thus spatial variations are constrained. We performed a grid search along the zeroth-, first-, and second-derivative weights for the combination of parameters to provide a smooth solution with the smallest residuals.

To test the resolution of the PV network, we performed a checkerboard analysis (see Fig. 9a–c), using a 2D spatial grid that covered the area of interest with an interspacing distance of 130 m. Travel times are computed (see ray-path density in Fig. 9b) and the inversion is performed (see results in Fig. 9c). Checkerboard results suggest that reliable velocities are estimated for the area enclosed by the stations. The section of inverse solution with no ray coverage is masked in white.

The tomographic inversion procedure is applied to the retrieved GFs to each frequency between 0.8 and 4 Hz at a 0.1 Hz interval. The results for 1–3 Hz are shown in Figure 9d, 9e, and 9f, respectively. These results indicate higher velocities at the northeast and the southwest side of the PV-array area for all the frequencies.

Figure 10 shows a histogram of the time residuals of all the traced ray paths; that is, from all the station pairs for all the frequencies of the tomographic solution. As expected,

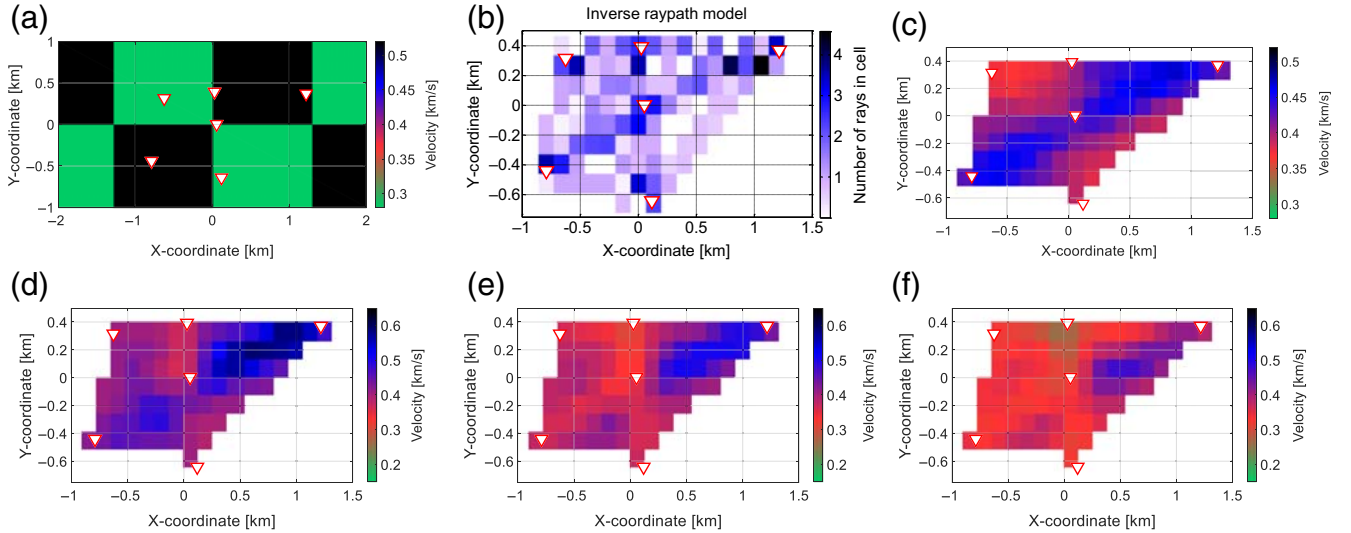


**Figure 9.** Utilization of PRONTO software. (a) Proposed velocity model for the checkerboard analysis. (b) Ray-path density per inversion cell. (c) Inversion for the velocity model proposed in (a). (d–f) Inversion of retrieved Green’s functions for 1, 2, and 3 Hz, respectively. The color version of this figure is available only in the electronic edition.

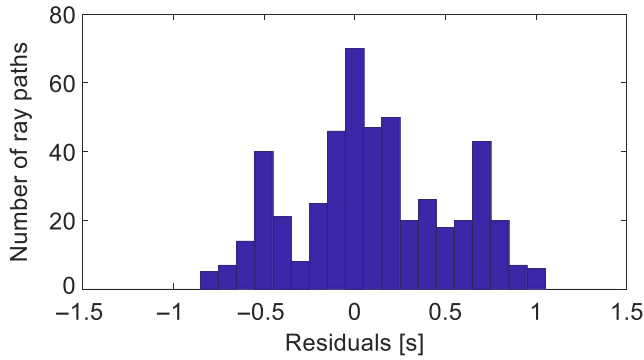


**Figure 10.** Histogram of the time residuals from all the station pairs for all the frequencies of the tomographic solution. The color version of this figure is available only in the electronic edition.

most of the time residuals are close to zero seconds. The smallest time residuals are in the frequency band [1, 3] Hz. For some frequencies, the inversion is not well constrained due to the small number of stations, which implies a small number of rays and their incidence angles on each of the inversion cells. Therefore, Figure 10 differs from a Gaussian distribution. Even though the maximum residuals are around 1 s, they are just  $\sim 5\%$  of the amount of ray paths that converged to 0 s and are relevant to the highest frequencies of the inversion procedure. Thus, the results are sufficiently reliable. A larger number of rays with a broad range of incidence angles are required over the area of interest to obtain a well-constrained high-resolution result. Nevertheless, this work provides a reliable first estimation of the  $S$ -wave velocities for the area.

## Depth Inversion

The inversion procedure by which surface-wave DCs are employed to retrieve the  $S$ -wave velocity distribution as a function of depth was performed using the procedure developed by [Haney and Tsai \(2017\)](#). We adapted their procedure for processing a grid of DCs, which are obtained from the tomographic solution. With this procedure, for the solution of the forward problem, surface-wave velocities are computed with the eigenvalue/eigenvector method proposed by [Lysmer \(1970\)](#). According to the method, layers must be thin relative to the wavelength to ensure accuracy. The inversion is based on the work of [Kausel \(2005\)](#), who uses the finite-element method to derive a matrix formulation of the forward problem. Then, the inverse problem can be solved using matrix perturbation theory. An initial model is provided by use of the nonperturbational Rayleigh-wave inversion introduced by [Haney and Tsai \(2015\)](#). Given a sufficiently large number of layers, the standard deviation of the observed data, and the chi-squared boundary values to constrain the acceptable models, the inversion of [Haney and Tsai \(2015\)](#) is designed to provide an estimate of the overall behavior of the true model by utilization of a weighted-damped least-squares regularization.

The grid of points previously utilized to obtain the tomographic images (see the [Rayleigh-Wave Tomography](#) section) is used in the inversion procedure for the retrieval of the  $S$ -wave velocities. At each point in the grid, the tomographically derived group velocities are extracted. In this way, we have a group velocity DC at each grid point. Each DC is then inverted for  $S$ -wave velocity with depth. A non-uniform layering for Rayleigh-wave inversion is performed using the initial phase-velocity DC. We used 30 layers down

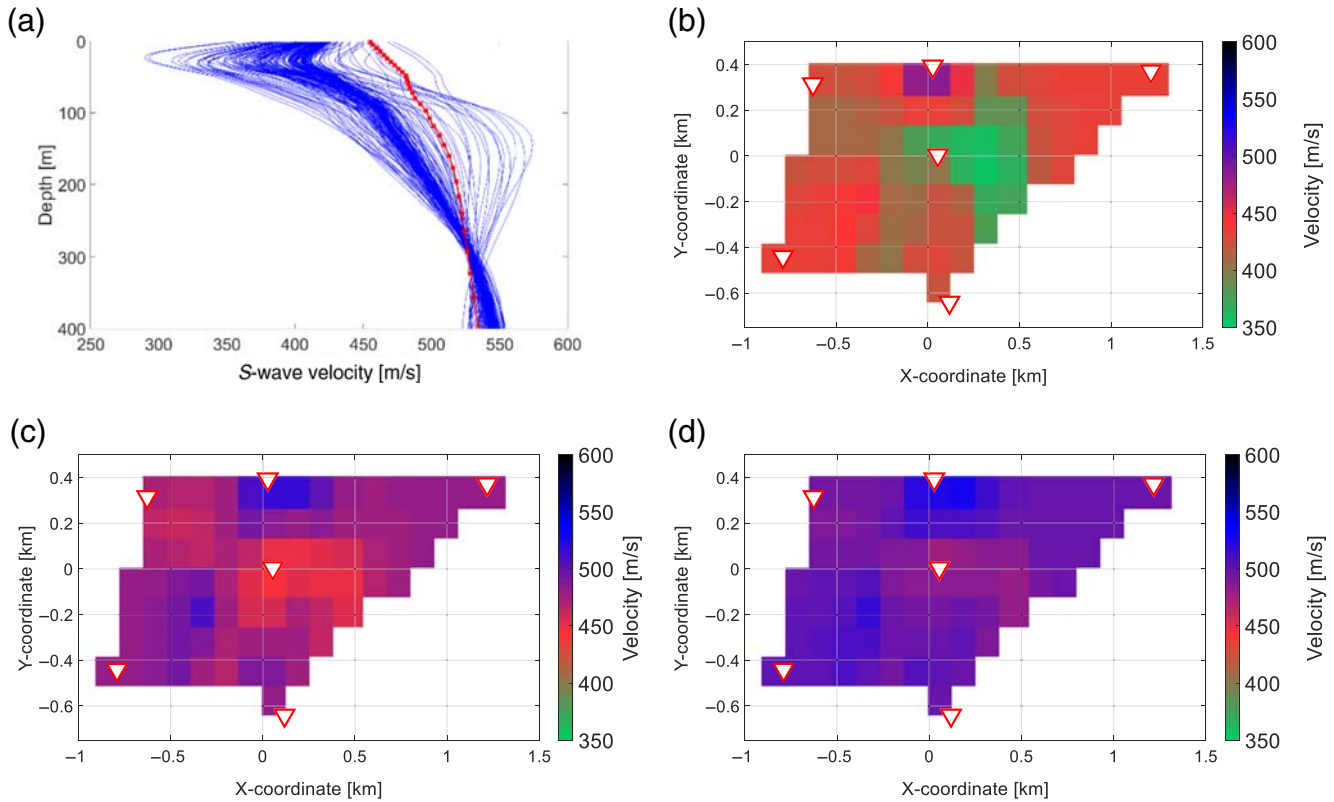


**Figure 11.** Results of the  $S$ -wave inversion procedure. (a)  $S$ -wave velocity profiles for each of the grid points of the area under study. The curve marked with squares depicts the initial model for the inversion. (b–d)  $S$ -wave velocity distribution at a depth of 60, 140, and 200 m, respectively. The color version of this figure is available only in the electronic edition.

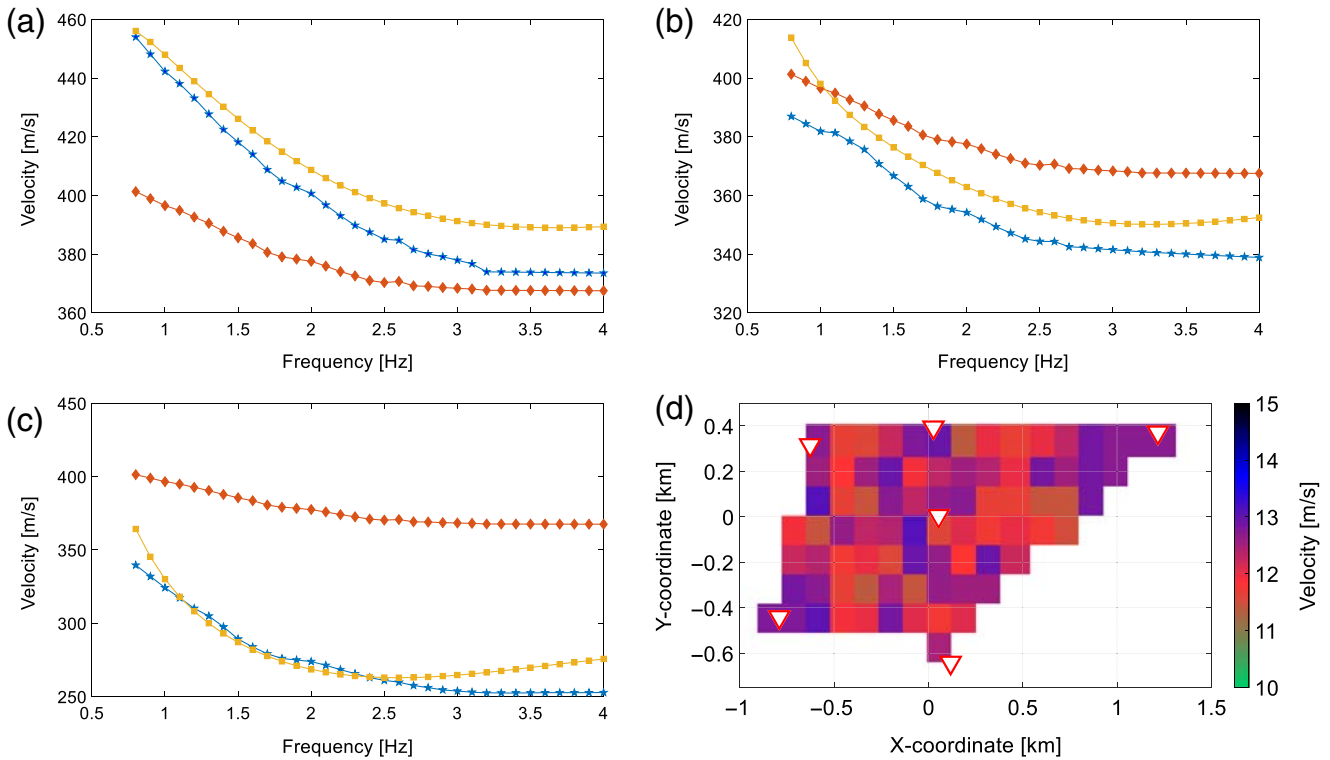
to a depth of 500 m (hereafter, inversion layers), so that these layers are thin enough compared with the working wavelengths. The selection of 30 inversion layers in the first 500 m is an initial condition for the applied methodology to accurately converge during the inversion. From the initial model, perturbations in phase velocity are related to perturbations in material properties at each iteration, resulting in the relatively smooth  $S$ -wave velocity profiles. The results are shown in Figure 11a–d. This methodology provides an overall velocity estimate for the actual subsurface; thus, a particular velocity value for one of the proposed inversion layers is senseless without considering the surrounding velocity layers. This means that subsurface features are described by a group of inversion layers. To show the velocity changes with depth, Figure 11a presents all of the  $S$ -wave velocity profiles (solid curves) and the initial model (squares). The same initial model was used for every grid-point inversion because the  $S$ -wave velocity changes are not expected to be large, which is supported by the obtained velocity profiles. Figure 11a leads to the interpretation of two layers for the subsurface down to the investigation depth limit of about 350 m. The shallower layer is located in the first 70 m of the subsurface and is characterized by a low velocity, that is, 300–400 m/s. From 70 m to (at least) 350 m depth, a higher velocity layer is present ranging from 450 to 570 m/s. Figure 11a also shows that the shape of the curves are similar among the nodes.

Figure 11b–d exhibits the spatial distribution of velocities at several depths. The images from the different depths indicate that the higher velocities are located at the north and southwest of the area enclosed by the stations. In addition, the second high-velocity regions are located at the very south and the northeast of the array. In accordance, a low-velocity band is retrieved for the area between the high-velocity zones.

Figure 12 shows the quality of the depth-inversion solution. Figure 12a–c presents the observed DC, the initial DC for the inversion algorithm (the same curve for every DC to invert), and the DC associated with the final depth-inversion solution for the grid points containing three of the stations of the array (i.e., PV02, PV03, and PV06). The final solution fits the data under acceptable parameters, which are defined by the uncertainties in the observed data. Figure 12d shows the distribution of root mean square (rms)  $S$ -wave velocity errors for the area enclosed by the stations. Figure 12 indicates that the final solution is a good solution to predict the data, as the rms values do not exceed 14 m/s.

### Interpretation of Results and Discussion

Several studies reported similar velocity values in volcanic areas, for example, Petrosino *et al.* (2002) at Stromboli, Italy; Saccorotti *et al.* (2003) at Kilauea, U.S.A.; and Mora



**Figure 12.** (a–c) Observed dispersion curve (stars), initial Rayleigh-wave velocity model for depth inversion (diamonds), and dispersion curve of the final depth-inversion solution (squares) for the grid points containing stations PV02, PV03, and PV06, respectively. (d) Root mean square (rms)  $S$ -wave velocity errors for the area enclosed by the stations. The color version of this figure is available only in the electronic edition.

*et al.* (2006) at Arenal, Costa Rica. In particular, Saccorotti *et al.* (2003) state that in spite of the differences in the lithological settings across volcanoes worldwide, for those dominated by volcanic sediments at the surface, the retrieved velocity structure of their shallower subsurface (i.e., down to  $\sim 500$  m) remains fairly constant. Although this assertion does not by itself validate our results, it is used as a reference for the probable velocities retrieved in the area of the PV-array.

The resolution of the obtained velocity results is limited by the geological conditions and the acquisition geometry. The first is defined by the inherent high complexity of the studied active volcanic area (e.g., compositional, structural, porosity, lithology, and fluid-content variations); the second is described by the limitations imposed by the recording array and source distribution (e.g., number of stations, their distribution, and the useful frequency range). The applied methodology is appropriate to these particular initial geological and acquisition conditions, as it provides an overall velocity estimate for the actual subsurface. Therefore, interpretations are based on the overall behavior of the velocity values.

The limited geological information available for the area of the PV-array (Lemus Hernandez, 2010; Tapia Silva, 2010) indicates a subsurface composed of eroded lavas and pyroclastic rocks (basaltic, dacitic, and andesitic material) in its

shallower part, which is down to more than  $\sim 100$  m from the surface, followed by andesitic–basaltic volcanic sediments in its deeper part, which is  $\sim 200$  m thick. These are the Volcán Peteroa-Azufre and Cola de Zorro formations, respectively. We interpret our results (see Fig. 11a) as representing these two shallow units, which show slight velocity changes in the area (see Fig. 11b–d). Limited information exists about the characteristics of the subsurface beneath the PV-array. Therefore, based on the inherent heterogeneity of this volcanic area, we cannot discard the possibility that slight horizontal changes in lithology (caused by lateral variations of the subsurface materials—in the same layer, or between layers likely due to the nonhomogeneous thicknesses of the layers—or due to structural features like faulting), porosity, portion of the rock saturated by fluid, or type of fluids saturating the porous rock contribute to the observed velocity variations.

Volcanic rocks present a great variety of porosity types. According to the genesis of the rocks, these types are classified in primary, associated with the origin of the rock, or secondary, associated with the interaction between the rock and its environment (Sruoga and Rubinstein, 2007). In the case of primary-porosity rocks, a change in porosity for values higher than a threshold (i.e., higher than the critical porosity of the rock) causes a very small velocity change; to the contrary, for porosities lower than this threshold, significant velocity variations are observed as a result of a relatively small porosity

variation (Mukerji and Mavko, 2006). As an example of the effect of secondary-type porosity, Zamora *et al.* (1994) show that the *S*-wave velocity due to vesicular and fissural features in the same volcanic material differ even by 30%. Volcanic areas generally present a combination of porosity types, leading to a wide range of porosity values. Therefore, specific characterization of porosity features in the area is required to, at least, constrain the likely velocity variations due to porosity.

Differential saturation in a porous rock might cause significant velocity changes. Zamora *et al.*, (1994) estimates a maximum *S*-wave velocity variation of ~20% between the dry and water-saturated rock in the first kilometer of the subsurface in Campi Flegrei, Italy; Adam and Otheim (2013) model velocity variations in a porous basalt rock and identify variations of ~10% when water is replaced by liquid CO<sub>2</sub>. Several studies have also estimated velocity variations lower than 10% (e.g., Entwisle *et al.*, 2005; Vanorio *et al.*, 2002). Nevertheless, laboratory measurements use ultrasonic frequencies. At these frequencies (i.e., 0.1–1 MHz), velocity values are affected by dispersion and scattering processes different from those present at the seismic frequencies relevant to typical volcanology studies (i.e., 0.1–10 Hz; Lesage *et al.*, 2018). Then, calculated velocities are only a rough estimate of the actual seismic velocities.

Based on the works of Benavente *et al.* (2015) and Tassi *et al.* (2016), the circles in Figure 3 indicate the location of several thermal manifestations in the area (i.e., hot springs, bubbling pools, mud pools, fumaroles, and/or steaming grounds). Table 1 (extracted from Tassi *et al.*, 2016) shows the results of the analysis for the volcanic fluids collected at each sample point. Some of these thermal points are located along the west side of the PV-array (those described in Table 1). The geochemical analysis of the fluids collected at the western area reflects a subsurface locally saturated by water. Even though no estimates of the dimensions of the water-saturated rock volume have been provided in Tassi *et al.* (2016), there is no physical reason to think that this volume is confined solely to the point where the gas samples were captured. Therefore, along the western zone of the PV-array, the saturated volume has a strong correlation with the location of low *S*-wave velocity values. Given a porous rock saturated by at least ~15% of gas, it has been observed (Toksoz *et al.*, 1976; Hamada, 2004) that nearly all of the shear deformation is absorbed by the porous portion. Thus, the shear modulus is hardly affected causing the *S*-wave velocity changes to be largely related to density changes. Then, a significant percentage of the reduction in velocity in the western area of the PV-array is potentially related to the existence of hydrothermal fluids and associated chemical processes. The chemical processes associated with hydrothermal fluid flow alter the lithology and porosity of the rock (Pola *et al.*, 2012). Thus, the most probable scenario for the western area of the PV-array is a subsurface characterized by particular saturation, lithology, and porosity conditions.

In volcanic areas, physical parameters (such as porosity and saturation) present a wide range of possible values.

Table 1

Geochemical Information of the Planchón-Peteroa Volcanic Complex (PPVC) Gas Discharges at the Sampling Points Located Along the Western Side of the PV-Array (Tassi *et al.*, 2016)

| ID   | Type          | Date          | Latitude | Longitude | Altitude | T    | CO <sub>2</sub> | HCl    | HF      | SO <sub>2</sub> | H <sub>2</sub> S | N <sub>2</sub> | CH <sub>4</sub> | Ar   | O <sub>2</sub> | H <sub>2</sub> | He     | CO       | X <sub>gas</sub> % |
|------|---------------|---------------|----------|-----------|----------|------|-----------------|--------|---------|-----------------|------------------|----------------|-----------------|------|----------------|----------------|--------|----------|--------------------|
| Gen1 | Bubbling pool | February 2010 | 6098170  | 362325    | 2472     | 26.3 | 990             | < 0.01 | < 0.005 | < 0.01          | < 0.01           | 8.1            | 1.4             | 0.15 | 0.55           | 0.0048         | 0.0078 | < 0.0005 | 98.5               |
| Gen2 | Bubbling pool | February 2010 | 6098014  | 362203    | 2476     | 28.2 | 993             | < 0.01 | < 0.005 | < 0.01          | < 0.01           | 5.3            | 1.3             | 0.12 | 0.62           | 0.0061         | 0.0052 | < 0.0005 | 98.7               |
| Gen2 | Bubbling pool | March 2012    | 6098014  | 362203    | 2476     | 28.2 | 993             | < 0.01 | < 0.005 | < 0.01          | < 0.01           | 5.3            | 1.1             | 0.13 | 0.62           | 0.0061         | 0.0052 | < 0.0005 | 93.5               |
| Gen2 | Bubbling pool | March 2015    | 6098014  | 362203    | 2476     | 24.1 | 992             | < 0.01 | < 0.005 | < 0.01          | < 0.01           | 5.6            | 1.3             | 0.14 | 0.55           | 0.0035         | 0.0031 | < 0.0005 | 94.1               |

Type of manifestation, sampling date, geographical coordinates (UTM, WGS 85 Zone 19), altitude (m.a.s.l.), outlet temperatures (in °C), chemical composition (dry gas fraction) of inorganic gases and CH<sub>4</sub> (in mmol/mol), and total concentration of the dry gas fraction (X<sub>gas</sub> in %) are provided.

Therefore, the association of seismic results to the physical features present in an area requires, at least, a constraint to the physical parameters, which is achieved by specific analyses of the rock properties.

The spatial *S*-wave velocity contrasts are roughly preserved in depth at least down to the investigation depth limit (i.e., about 350 m), which guides us to hypothesize that the contrast of subsurface characteristics in the area is similar at these depths. Nevertheless, one should note that the closer to the maximum depth of investigation, the less sensitive the results are to subsurface parameters. Thus, velocity contrasts could be slightly underestimated at these depths. In addition, the low *S*-wave velocity values extend from the western area through the center of the array and to the southern section. The observed velocity distribution indicates that the subsurface characteristics (i.e., lithology, porosity, and saturation of the rocks and its dominant components—gas or water) are probably similar along the *S*-wave low-velocity belt. Furthermore, we interpret the higher velocity values as zones characterized by variations in the composition of the layers (due to depositional or structural causes), or porosity, and/or a reduction of water content (likely replaced by gas); each of them contribute to enhance the *S*-wave velocities variations. Nevertheless, it is clear that further geochemical, geophysical, and geological studies are required to develop a complete and accurate understanding of the subsurface characteristics.

Forecasting of volcanic behavior is a multidisciplinary process based on analytical studies of volcanic samples, experimental investigations, theoretical modeling of the dynamic magmatic systems, and simulation of the geophysical signals, eruptive behaviors, and hazardous phenomena (Sparks, 2003). These studies require a constraint of the implicated variables (e.g., lithology, structures, porosity, type and saturation of fluids, and proximity of a water reservoir to a magma batch, among other variables) that influence the physical–chemical processes occurring in the volcanic area. Thus, knowledge of subsurface characteristics is essential to subsequently obtain an accurate forecast of volcanic behavior.

No accurate forecasts have been developed at Peteroa yet, likely a consequence of insufficient information about its dynamics geology subsurface properties and processes. Our results do not suggest a direct explicit improvement in forecasting at Peteroa. However, results are a contribution to the knowledge of the subsurface of a poorly understood region located at the east of the active volcano. This contribution is expected to be used by imminent future studies for the characterization of the area, and, in a second step, for specific studies aimed to forecast the Peteroa dynamics. Our results are also expected to be used by characterization studies that precede mitigation risk analyses, as knowledge of the subsurface mechanical properties, structures, lithology, porosity, fluid content, among other variables, are relevant information in defining the hazardous areas located around a volcano (Tilling, 1989; Felpeto *et al.*, 2007).

## Conclusions

The accepted mechanism by which the PPVC developed their last eruptions is the development of fractures, which caused pressure changes and consequently the movement of fluids toward the surface. The western part of the target area present fluid manifestations and a subsurface saturated by water. Previous works interpret the likely presence of magma approaching the area, which warrants the importance of its study. Furthermore, several measurements of surface observables are performed in the area of the Peteroa. Knowledge of the subsurface parameters could further understanding of the surface activity and thus improve the decisions of the local authorities in cases of a volcanic unrest.

We applied SI to ambient-noise data recorded by a seismic array of six stations from the temporary network MalARRgue, which recorded ambient noise in 2012 in the Malargüe region, Mendoza, Argentina. The six stations we used were located along the eastern flank of the Peteroa Volcano, the current active edifice of the PPVC, to retrieve the *S*-wave velocity structure down to about 350 m. We analyzed the main directions of the ambient-noise wavefield at each time window during the recording period. For application of SI, we then selected the station pairs whose stationary-phase area for ballistic surface waves was aligned with one of the main directions of the noise. Therefore, we assured the retrieval of more accurate surface-wave GFs. Using the retrieved ballistic Rayleigh-wave arrivals, we measured the group-velocity DCs, which were used to obtain spatial maps of surface-wave velocities through a frequency-dependent tomographic inversion. The retrieved velocity values are coherent and match the estimation of the average surface-wave velocity for the area derived from local earthquakes. Dispersion inversion across the tomographic grid was performed to obtain the 3D *S*-wave velocity structure. From these inversions, we infer the presence of two layers. The shallower layer is located from the surface down to about 70 m depth and is characterized by *S*-wave velocities between 300 and 400 m/s. The second layer extends at least down to about 350 m depth with *S*-wave velocities increasing with depth from 450 to 570 m/s. These two layers correspond to the first two units of the stratigraphic column describing the study area. Slices at different depth values indicate zones of higher and lower *S*-wave velocity that are relatively consistent in depth, at least down to about 350 m. This is confirmed by the profiles shown in Figure 11a. Even though the magnitude of the velocity contrasts slightly varies with depth, it is clear that the sign of the contrasts remains constant for the majority of the profiles. It means that the local maximum and minimum values do not change along depth. Higher velocities are located at the northeast and the very southwest parts of the area enclosed by the stations. Lower velocities are situated in between, along a northwest–southeast-trending feature.

The intrinsic heterogeneity of this volcanic complex, in addition to the close proximity of sample points that have geochemical analyses and a portion of the area with low *S*-wave velocities, leads to a joint geological interpretation.

We interpret the velocity variations as caused by the contribution of compositional changes, the presence of structural features (e.g., faults), porosity changes, and/or differential saturation of the porous rock. Nevertheless, the limited available geological information in the zone is not sufficient to accurately estimate the percentages due to each contribution. The western zone of the area under study is characterized by a subsurface locally saturated by water. The subsurface characteristics (lithology, porosity, dominant type of fluid—gas or water—and saturation of the fluids in rocks) are likely similar along the low *S*-wave velocity area.

The results contribute to the knowledge of the subsurface properties of the PPVC. This information is to be used by characterization studies which precede volcanic risk analyses and forecasting investigations.

Estimating the velocities along a wide range of depths requires a broadband of frequencies and interstation distances. *S*-wave velocities of the subsurface down to about 350 m were estimated using interstation distances between 0.4 and 2.1 km and frequencies from 0.8 to 4 Hz. We propose that future works complement the results obtained in this study through the application of SI to records from an array with higher interstation distances to estimate deeper *P*- and *S*-wave velocities, in particular to the depths expected for the location of the magmatic reservoirs in the PPVC.

### Data and Resources

The seismic records utilized in this work were provided by the Malargüe seismic array (MalARRgüe project). The data are freely available and can be downloaded from the database of Incorporated Research Institutions for Seismology (IRIS). Maps were created with Global Mapping Tools (GMT, v.5.2.1) and Maptitude software (Student–Teacher License SW, v.2017). Deconvolution was applied by utilization of Portable Data Collection Center toolkit (PDCC, IRIS) and the ObsPy Python-based programming package. The script for the polarization analysis was provided by Martin Schimmel, programmed with GNU Fortran. The computation of the cross correlations and the dispersion curves, the tomographic inversion, and the inversion for the *S*-wave velocities were performed offline combining a commercial software package (MATLAB, the MathWorks, Inc., Natick, Massachusetts, available at [www.mathworks.com/products/matlab](http://www.mathworks.com/products/matlab), last accessed February 2018) and GNU Fortran.

### Acknowledgments

J. A. Casas thanks Facultad de Ciencias Astronómicas y Geofísicas de La Plata (FCAGLP) and Boise State University (BSU) for providing working facilities. The authors thank Matthew Haney and Victor Tsai for providing the *S*-wave velocity inversion software. The research of D. Draganov is supported by the Division for Earth and Life Sciences (ALW) with financial aid from the Netherlands Organization for Scientific Research (NWO) with Grant Number VIDI 864.11.009. The authors thank Incorporated Research Institutions for Seismology–Program for the Array Seismic Studies of the Continental Lithosphere (IRIS-PASSCAL) for providing the seismic equipment and the Argentine Ministry of Science, Technology and Production

Innovation for the financial support connected to the transportation of the equipment. The authors also thank Pierre Auger Observatory and the Department of Civil Defense of Malargüe for the help during the data acquisition. The authors also thank Mariano Agosto for his kindly discussion about the geochemical interpretation of the results. The authors thank two anonymous reviewers and Associate Editor Thomas Pratt, for their comments that helped improve the article.

### References

- Adam, L., and T. Otheim (2013). Elastic laboratory measurements and modeling of saturated basalts, *J. Geophys. Res.* **118**, no. 3, 840–851.
- Aguilera, F., O. Benavente, F. Gutiérrez, J. Romero, O. Saltori, R. González, M. Agosto, A. Caselli, and M. Pizarro (2016). Eruptive activity of Planchón-Peteroa volcano for period 2010–2011, southern Andean volcanic zone, Chile, *Andean Geol.* **43**, no. 1, 20–46, doi: [10.5027/andgeoV43n1-a02](https://doi.org/10.5027/andgeoV43n1-a02).
- Agusto, M., M. C. Lamberti, N. Núñez, H. Sánchez, S. García, and M. Gómez (2017). Primeros datos de desgasificación difusa de CO<sub>2</sub> de la caldera del Volcán Planchón-Peteroa, *Proc. of the XII Meeting of the International Center for Earth Sciences*, 103 pp., ISBN: 978-987-1323-49-4 (in Spanish).
- Aki, K., and P. G. Richards (1980). *Quantitative Seismology*, W. H. Freeman and Company, New York, New York.
- Aldridge, D. F., and D. W. Oldenburg (1993). Two-dimensional tomographic inversion with finite-difference traveltimes, *J. Seismic Explor.* **2**, 257–274.
- Almendros, J. (1999). Análisis de señales sismovolcánicas mediante técnicas de array, *Tesis doctoral*, Instituto Andaluz de Geofísica. Universidad de Granada, 301 pp. (in Spanish).
- Almendros, J., J. M. Ibáñez, G. Alguacil, E. Del Pezzo, and R. Ortiz (1997). Array tracking of the volcanic tremor source at the Deception Island, *Geof. Res. Lett.* **24**, no. 23, 3069–3072.
- Benavente, O., F. Tassi, M. Reich, F. Aguilera, F. Capecciacci, F. Gutierrez, O. Vaselli, and A. Rizzo (2015). Chemical and isotopic features of cold and thermal fluids discharged in the southern volcanic zone between 32.5S and 36S: Insights into the physical and chemical processes controlling fluid geochemistry in geothermal systems of central Chile, *Chem. Geol.* doi: [10.1016/j.chemgeo.2015.11.010](https://doi.org/10.1016/j.chemgeo.2015.11.010).
- Benavente Zolezzi, O. (2010). Actividad Hidrotermal asociada a los Complejos Volcánicos Planchón-Peteroa y Descabezado Grande-Quizapu-Cerro Azul, 36°S y 37°S, Zona Volcánica Sur, Chile, *Master Thesis*, Universidad de Chile, 204 pp. (in Spanish).
- Bensen, G. D., M. H. Ritzwoller, M. P. Barmin, A. L. Levshin, F. Lin, M. P. Moschetti, N. M. Shapiro, and Y. Yang (2007). Processing seismic ambient noise data to obtain reliable broad-band surface wave dispersion measurements. *Geophys. J. Int.* **169**, 1239–1260, doi: [10.1111/j.1365-246X.2007.03374.x](https://doi.org/10.1111/j.1365-246X.2007.03374.x).
- Bensen, G. D., M. H. Ritzwoller, and N. M. Shapiro (2008). Broadband ambient noise surface wave tomography across the United States, *J. Geophys. Res.* **113**, no. B05306, doi: [10.1029/2007JB005248](https://doi.org/10.1029/2007JB005248).
- Bonnefoy-Claudet, S., F. Cotton, and P. Bard (2006). The nature of noise wavefield and its application for site effects studies: A literature review, *Earth Sci. Rev.* **79**, 205–277.
- Brenguier, F., N. Shapiro, M. Campillo, A. Nercessian, and V. Ferrazzini (2007). 3-D surface wave tomography of the Piton de la Fournaise volcano using seismic noise correlations, *Geophys. Res. Lett.* **34**, no. 2, 2305.
- Campillo, M., and A. Paul (2003). Long-range cross correlations in the seismic coda, *Science* **299**, 547–549.
- Casas, J. A., G. Badi, M. C. Manassero, P. Gomez, D. Draganov, and J. Ruzzante (2014). Characterization of seismo-volcanic activity in Peteroa Volcano, central Andes Argentina-Chile, special issue, *Earth Sci. Res. J.* **18**, 335–336, ISBN: 1794–6190.

- Cembrano, J., and L. Lara (2009). The link between volcanism and tectonics in the southern volcanic zone of the Chilean Andes: A review, *Tectonophysics* **471**, nos. 1/2, 96–113.
- De Meersman, K., M. Van der Baan, and J.-M. Kendall (2006). Signal extraction and automated polarisation analysis of multi-component array data, *Bull. Seismol. Soc. Am.* **96**, 2415–2430.
- Draganov, D., and E. Ruigrok (2015). Passive seismic interferometry for subsurface imaging, *Encyclopedia Earthq. Eng.* doi: [10.1007/978-3-642-36197-5\\_378-1](https://doi.org/10.1007/978-3-642-36197-5_378-1).
- Entwisle, D. C., P. R. N. Hobbs, L. D. Jones, D. Gunn, and M. G. Raines (2005). The relationships between effective porosity, uniaxial compressive strength and sonic velocity of intact Borrowdale Volcanic Group core samples from Sellafeld, *Geotech. Geol. Eng.* **23**, no. 6, 793–809.
- Escudero, C. R., and W. L. Bandy (2017). Ambient seismic noise tomography of the Colima Volcano Complex, *Bull. Volcanol.* **79**, no. 13, doi: [10.1007/s00445-016-1096-2](https://doi.org/10.1007/s00445-016-1096-2).
- Felpeo, A., J. Martí, and R. Ortiz (2007). Automatic GIS-based system for volcanic hazard assessment, *J. Volcanol. Geoth. Res.* **166**, no. 2, 106–116.
- Fournier, R. (2007). Hydrothermal systems and volcano geochemistry, in *Volcano Deformation-Geodetic Monitoring Techniques*, D. Dzurisin (Editor), Springer-Praxis Books in Geophysical Sciences, Berlin, Germany, 323–341.
- Frankel, A., S. Hough, P. Friberg, and R. Busby (1991). Observations of Loma Prieta aftershocks from a dense array in Sunnyvale, California, *Bull. Seismol. Soc. Am.* **81**, 1900–1922.
- Gill, J. B. (1981). *Orogenic Andesites and Plate Tectonics*, Springer-Verlag, New York, New York.
- Godin, O. A. (2006). Recovering the acoustic Green's function from ambient noise cross correlation in an inhomogeneous moving medium, *Phys. Rev. Lett.* **97**, 054301.
- Haller, M. J., H. A. Osters, A. H. Pesce, M. Gardini, and A. Folgueras (1994). Vulcanoestratigrafía reciente y erupción del volcán Peteroa, *Congreso Geológico Chileno, N 7, Concepción, Actas 1*, 319–323 (in Spanish).
- Halliday, D. F., A. Curtis, J. O. A. Robertson, and D. J. van Manen (2007). Interferometric surface-wave isolation and removal, *Geophysics* **72**, A67–A73.
- Hamada, G. M. (2004). Reservoir fluids identification using  $V_p/V_s$  ratio, *Oil Gas Sci. Technol.-Rev. IFP* **59**, no. 6, 649–654.
- Haney, M. M., and V. C. Tsai (2015). Nonperturbational surface-wave inversion: A Dix-type relation for surface waves, *Geophysics* **80**, no. 6, EN167–EN177, doi: [10.1190/geo2014-0612.1](https://doi.org/10.1190/geo2014-0612.1).
- Haney, M. M., and V. C. Tsai (2017). Perturbational and nonperturbational inversion of Rayleigh-wave velocities, *Geophysics* **82**, no. 3, F15–F28, doi: [10.1190/GEO2016-0397.1](https://doi.org/10.1190/GEO2016-0397.1).
- Kausel, E. (2005). Wave propagation modes: From simple systems to layered soils, in *Surface Waves in Geomechanics: Direct and Inverse Modeling for Soil and Rocks*, C. G. Lai and K. Wilmanski (Editors), CISM International Centre for Mechanical Sciences (Courses and Lectures), Vol. 481, Springer, Vienna, Austria, 165–202.
- Kästle, E. D., R. Soomro, C. Weemstra, L. Boschi, and T. Meier (2016). Two-receiver measurements of phase velocity: Cross-validation of ambient-noise and earthquake-based observations, *Geophys. J. Int.* **207**, no. 3, 1493–1512, doi: [10.1093/gji/ggw341](https://doi.org/10.1093/gji/ggw341).
- Lemus Hernandez, M. G. (2010). Análisis Termal del Complejo Volcánico Descabezado Grande y Planchon Peteroa Mediante Sensores Remotos, *Graduate Thesis*, Universidad de Chile (in Spanish).
- Lesage, P., M. Heap, and A. Kushnir (2018). A generic model for the shallow velocity structure of volcanoes, *J. Volcanol. Geoth. Res.* doi: [10.1016/j.jvolgeores.2018.03.003](https://doi.org/10.1016/j.jvolgeores.2018.03.003).
- Loughlin, S. C., R. S. J. Sparks, S. K. Brown, S. F. Jenkins, and C. Vye-Brown (2015). *Global Volcanic Hazards and Risk*, Cambridge University Press, Cambridge, United Kingdom.
- Lysmer, J. (1970). Lumped mass method for Rayleigh waves, *Bull. Seismol. Soc. Am.* **60**, 89–104.
- Mora, M. M., P. Lesage, B. Valette, G. E. Alvarado, C. Leandro, J.-P. Métaixian, and J. Dorel (2006). Shallow velocity structure and seismic site effects at Arenal volcano, Costa Rica, *J. Volcanol. Geoth. Res.* **152**, nos. 1/2, 121–139, doi: [10.1016/J.JVOLGEORES.2005.09.013](https://doi.org/10.1016/J.JVOLGEORES.2005.09.013).
- Mukerji, T., and G. Mavko (2006). *Recent Advances in Rock Physics and Fluid Substitution*, 2006 Special Edition, Vol. 31, CSEG, Calgary, Alberta, Canada.
- Mulargia, F. (2012). The seismic noise wavefield is not diffuse, *J. Acoust. Soc. Am.* **131**, no. 4, doi: [10.1121/1.3689551](https://doi.org/10.1121/1.3689551).
- Nakata, N., P. Boué, F. Brenguier, P. Roux, V. Ferrazzini, and M. Campillo (2016). Body and surface wave reconstruction from seismic noise correlations between arrays at Piton de la Fournaise volcano, *Geophys. Res. Lett.* **43**, doi: [10.1002/2015GL066997](https://doi.org/10.1002/2015GL066997).
- Naranjo, J. (2012). Principales etapas evolutivas holocenas del volcán Planchón y su reactivación relacionada al megasismo del 27 de Febrero de 2010, *Congreso Geológico Chileno*, no. 13, 440–441 (in Spanish).
- Nishitsuji, Y., E. Ruigrok, M. Gómez, and D. Draganov (2014). Global-phase H/V spectral ratio for imaging the basin in the Malargüe region, Argentina, *Seismol. Res. Lett.* **85**, 1004–1011, doi: [10.1785/0220140054](https://doi.org/10.1785/0220140054).
- Petrosino, S., P. Cusano, G. Saccorotti, and E. Del Pezzo (2002). Seismic attenuation and shallow velocity structures at Stromboli Volcano, Italy, *Bull. Seismol. Soc. Am.* **92**, no. 3, 1102–1116, doi: [10.1785/0120010147](https://doi.org/10.1785/0120010147).
- Picozzi, M., S. Parolai, D. Bindi, and A. Strollo (2009). Characterization of shallow geology by high-frequency seismic noise tomography, *Geophys. J. Int.* **176**, no. 1, 164–174, doi: [10.1111/j.1365-246X.2008.03966.x](https://doi.org/10.1111/j.1365-246X.2008.03966.x).
- Pola, A., G. Crosta, N. Fusi, V. Barberini, and G. Norini (2012). Influence of alteration on physical properties of volcanic rocks, *Tectonophysics* **566**, 67–86.
- Raponi, M., S. García, M. Gómez, and M. Agosto (2017). Mediciones remotas de SO<sub>2</sub> en el Complejo Volcánico Planchón-Peteroa, empleando un sistema DOAS portable, *Proc. of the XII Meeting of the International Center for Earth Sciences*, 83 pp., ISBN: 978-987-1323-49-4.
- Ruigrok, E., D. Draganov, M. P. Gomez, J. Ruzzante, D. Torres, I. Lopes Pumarega, N. Barbero, A. Ramirez, A. R. Castano Ganan, K. van Wijk, et al. (2012). Malargüe seismic array: Design and deployment for the temporary array, *Eur. Phys. J. Plus* **127**, doi: [10.1140/epjp/i2012-12126-7](https://doi.org/10.1140/epjp/i2012-12126-7).
- Saccorotti, G., B. Chouet, and P. Dawson (2003). Shallow-velocity models at the Kilauea Volcano, Hawaii, determined from array analyses of tremor wavefields, *Geophys. J. Int.* **152**, 633–648, doi: [10.1046/j.1365-246X.2003.01867.x](https://doi.org/10.1046/j.1365-246X.2003.01867.x).
- Schimmel, M., and J. Gallart (2004). Degree of polarization filter for frequency-dependent signal enhancement through noise suppression, *Bull. Seismol. Soc. Am.* **94**, no. 3, 1016–1035.
- Schuster, G. T. (2009). *Seismic Interferometry*, Cambridge University Press, New York, New York, ISBN: 13 978-0-511-54011-0.
- Shapiro, N. M., and M. Campillo (2004). Emergence of broadband Rayleigh waves from correlations of the ambient seismic noise, *Geophys. Res. Lett.* **31**, L07614, doi: [10.1029/2004GL019491](https://doi.org/10.1029/2004GL019491).
- Shen, Y., Y. Ren, H. Gao, and B. Savage (2012). An improved method to extract very-broadband empirical Green's functions from ambient seismic noise, *Bull. Seismol. Soc. Am.* **102**, no. 4, 1872–1877, doi: [10.1785/0120120023](https://doi.org/10.1785/0120120023).
- Snieder, R. (2004). Extracting the Green's function from the correlation of coda waves: A derivation based on stationary phase, *Phys. Rev. E* **69**, doi: [10.1103/PhysRevE.69.046610](https://doi.org/10.1103/PhysRevE.69.046610).
- Sparks, R. S. J. (2003). Forecasting volcanic eruptions, *Earth Planet. Sci. Lett.* **210**, nos. 1/2, 1–15.
- Sruoga, P., and N. Rubinstein (2007). Processes controlling porosity and permeability in volcanic reservoirs from the Austral and Neuquén basins, Argentina, *AAPG Bulletin* **91**, no. 1, 115–129.
- Stankiewicz, J., T. Ryberg, C. Haberland, Fauzi, and D. Natawidjaja (2010). Lake Toba volcano magma chamber imaged by ambient seismic noise tomography, *Geophys. Res. Lett.* **37**, L17306, doi: [10.1029/2010GL044211](https://doi.org/10.1029/2010GL044211).

- Tapia Silva, F. F. (2010). Análisis estructural del sector occidental de la faja plegada y corrida de Malargüe en el curso superior del río Colorado de Lontué (35°18' y 35°23' s), Región del Maule, Chile, *Graduate Thesis*, Universidad de Chile (in Spanish).
- Tassi, F., F. Aguilera, O. Benavente, A. Paonita, G. Chiodini, S. Caliro, M. Agosto, F. Gutierrez, B. Capaccioni, O. Vaselli, *et al.* (2016). Geochemistry of fluid discharges from Peteroa volcano (Argentina-Chile) in 2010–2015: Insights into compositional changes related to the fluid source region(s), *Chem. Geol.* doi: [10.1016/j.chemgeo.2016.04.007](https://doi.org/10.1016/j.chemgeo.2016.04.007).
- Tilling, R. I. (1989). Volcanic hazards and their mitigation: Progress and problems, *Rev. Geophys.* **27**, no. 2, 237–269.
- Toksoz, M. N., C. H. Cheng, and A. Timur (1976). Velocities of seismic waves in porous rocks, *Geophysics* **41**, no. 4, 621–645, doi: [10.1190/1.1440639](https://doi.org/10.1190/1.1440639).
- Tormey, D. R., F. A. Frey, and L. Lopez-Escobar (1989). Geologic history of the active Azufre-Planchón-Peteroa Volcanic Center (35°15' s, southern Andes) with implications for the development of compositional gaps, *Rev. Asoc. Geol. Argent.* **44**, nos. 1/4, 420–430.
- Vanorio, T., M. Prasad, D. Patella, and A. Nur (2002). Ultrasonic velocity measurements in volcanic rocks: Correlation with microtexture, *Geophys. J. Int.* **149**, no. 1, 22–36.
- Wapenaar, K., and J. Fokkema (2006). Green's function representations for seismic interferometry, *Geophysics* **71**, S133–S144.
- Wapenaar, K., and J. Thorbecke (2013). On the retrieval of the directional scattering matrix from directional noise, *J. Imaging Sci.* doi: [10.1137/12086131X](https://doi.org/10.1137/12086131X).
- Weemstra, K., D. Draganov, E. Ruigrok, J. Hunziker, M. Gomez, and K. Wapenaar (2017). Application of seismic interferometry by multidimensional deconvolution to ambient seismic noise recorded in Malargüe, Argentina, *Geophys. J. Int.* **208**, 693–714, doi: [10.1093/gji/ggw425](https://doi.org/10.1093/gji/ggw425).
- Xia, J., R. D. Miller, and C. B. Park (1999). Estimation of near-surface shear wave velocity by inversion of Rayleigh waves, *Geophysics* **64**, 691–700, doi: [10.1190/1.1444578](https://doi.org/10.1190/1.1444578).
- Xu, Z., and T. D. Mikesell (2017). On the reliability of direct Rayleigh-wave estimation from multicomponent cross-correlations, *Geophys. J. Int.* **210**, 1388–1393, doi: [10.1093/gji/ggx228](https://doi.org/10.1093/gji/ggx228).
- Zamora, M., G. Sartoris, and W. Chelini (1994). Laboratory measurements of ultrasonic wave velocities in rocks from the Campi Flegrei volcanic system and their relation to other field data, *J. Geophys. Res.* **99**, no. B7, 13,553–13,561.

## Appendix

### Estimate of the Average Surface-Wave Velocity Using Local Earthquakes

To validate the velocities obtained in this work by processing the noise data, we utilized the records of a group of local earthquakes to estimate the Rayleigh-wave velocities for the area enclosed by the PV-array (Kästle *et al.*, 2016). Using the Incorporated Research Institutions for Seismology (IRIS) Earthquake Browser, we selected seismic events that occurred in 2012 with magnitudes greater than  $M_w$  4 and depth less than 50 km (see Fig. A1). The events were chosen such that they are located roughly to the west of the PV-array (13 events for further processing and analysis), because it allowed a rough control of the direction of the seismic signals.

Extracting a window containing the surface waves for each event for each of the stations and filtering over the same frequency range as utilized for the noise data, we applied the maximum averaged cross correlation (MACC) method. MACC was developed by Frankel *et al.* (1991) and updated for volcanic areas by Almendros *et al.* (1997) and Almendros (1999). Casas *et al.* (2014) also applied MACC to estimate the apparent  $P$ -wave velocity in the area enclosed by the PV-array using the recorded volcano-tectonic events, resulting in an average apparent value of 1.1 km/s.

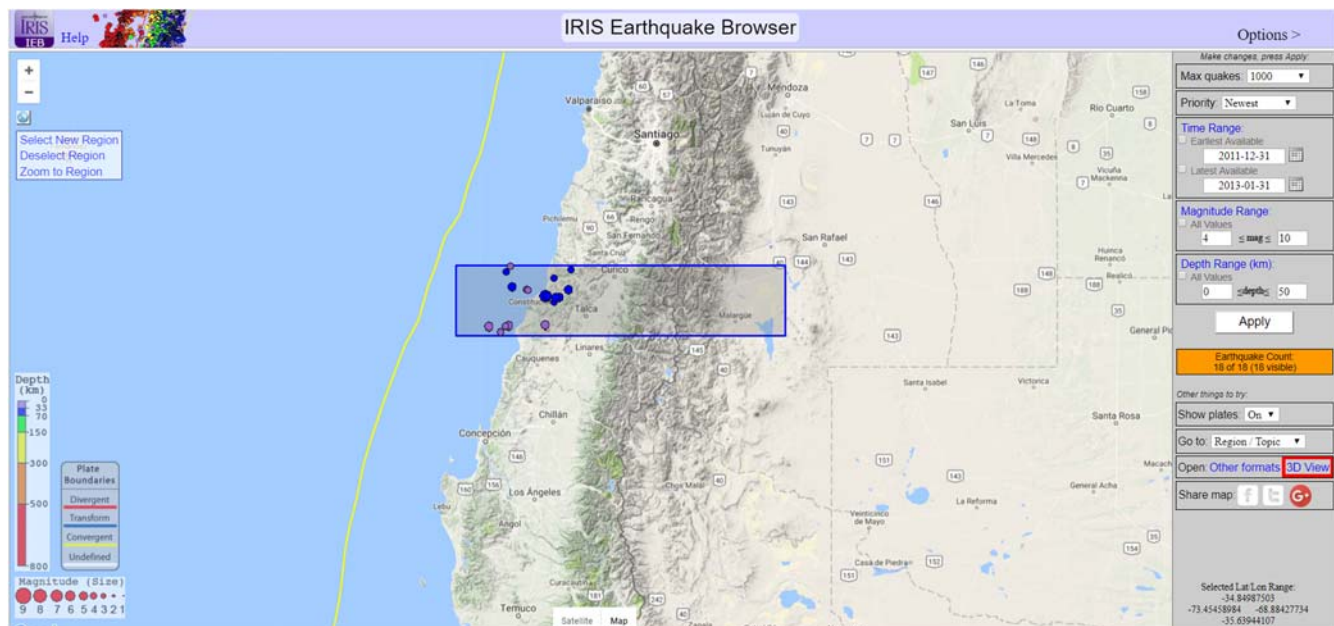


**Figure A1.** Local earthquakes used to estimate the average Rayleigh-wave velocity for the area enclosed by the PV-array. The color version of this figure is available only in the electronic edition.

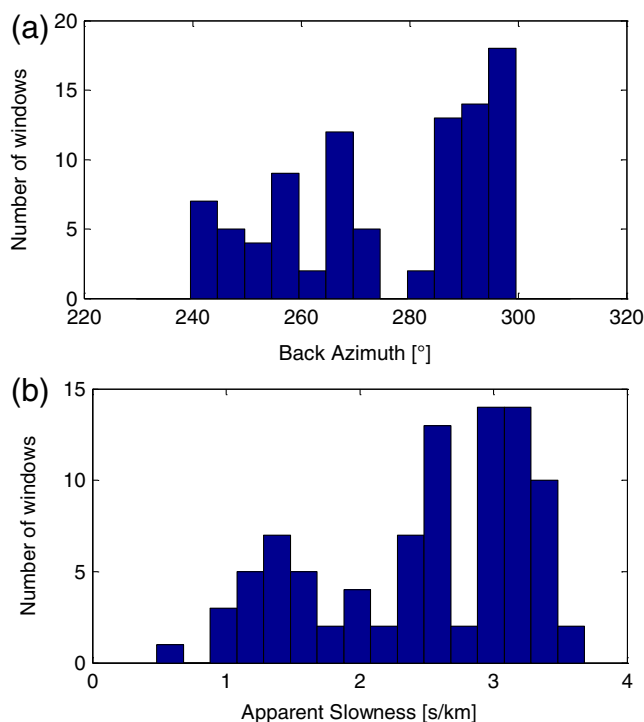


**Figure A2.** Results of the maximum averaged cross correlation (MACC) method. (a) Number of windows converged to back azimuth values and (b) number of convergent windows per apparent slowness. The color version of this figure is available only in the electronic edition.

Specifying a range of possible apparent slowness and back-azimuth values, a time-window length for correlation, a frequency range of processing, and the length of the data to use, MACC estimates the back azimuth of an event and the slowness of the waves propagating throughout the area enclosed by the stations. Naturally, the obtained slowness is related to the type of waves contained in the input data. Therefore, we used only input data, including the surface waves of the selected events.

MACC calculates the correlation coefficients of running correlation windows for all the possible back-azimuth and slowness values. From the selected events, correlation windows with the greatest correlation coefficients were accepted. No spatial filters were applied to the data before processing, so seismic energy arriving from any direction at those times would be also taken into account by the MACC method. It is clear that the energy released by the earthquakes is much greater than that of any ambient-seismic noise; however, the algorithm could also differentiate it. Then, to avoid windows dominated by waves coming from a direction different of that of the event, only waves with a back azimuth between  $240^\circ$  and  $300^\circ$  were selected. Finally, no constraints were applied to the slowness values of the correlation windows.

The results are shown in Figure A2. The presence of body waves propagating along the array might influence the time windows to converge at lower slowness values (higher velocities). Still, we observe that a majority of the windows

converge to slowness values between 2.25 and 3.5 s/km, or velocities of  $\sim 0.29$  and 0.45 km/s. An average value of 0.4 km/s is computed over the array. These results corroborate the velocities estimated from the noise correlations.

Facultad de Ciencias Astronómicas y Geofísicas  
Universidad Nacional de La Plata, CONICET  
Paseo del Bosque s/n  
B1900FWA  
Argentina  
acasas@fcaglp.unlp.edu.ar  
(J.A.C.)

Environmental Seismology Laboratory  
Department of Geosciences  
Boise State University  
1910 University Drive  
Boise, Idaho 83725-1535  
dylanmikesell@boisestate.edu  
(T.D.M.)

Department of Geoscience and Engineering  
Delft University of Technology  
Stevinweg 1, 2628 CN Delft  
The Netherlands  
d.s.draganov@tudelft.nl  
(D.D.)

Institute of Geophysics  
Faculty of Physics  
University of Warsaw  
ul. Pasteura 5, room B4.41  
02-093 Warszawa, Poland  
Simone. Lepore@fuw.edu.pl  
(S.L.)

Facultad de Ciencias Astronómicas y Geofísicas  
Universidad Nacional de La Plata  
Paseo del Bosque s/n  
B1900FWA  
Argentina  
gbadi@fcaglp.fcaglp.unlp.edu.ar  
(G.A.B.)

Observatorio Volcanológico de los Andes del Sur  
(OVDAS-SERNAGEOMIN)  
Rudecindo Ortega 03850  
Temuco, Chile  
luis.franco@sernageomin.cl  
(L.F.)

International Center for Earth Sciences  
Comision Nacional de Energía Atómica  
Avenida General Paz 1499, Buenos Aires  
Argentina  
mpgomez@cnea.gov.ar  
(M.G.)